

The 212.8-nm photodissociation of formic acid: Degenerate four-wave mixing spectroscopy of the nascent OH($X^2\Pi_j$) radicals

Keon Woo Lee, Kyoung-Seok Lee, and Kyung-Hoon Jung^{a)}

Department of Chemistry and School of Molecular Science (BK21), Korea Advanced Institute of Science and Technology, Taeduck Science Town, Taejeon 305-701, Korea

Hans-Robert Volpp

Physikalisch-Chemisches Institut der Universität Heidelberg, Im Neuenheimer Feld 253, D-69120 Heidelberg, Germany

(Received 20 February 2002; accepted 26 August 2002)

The 212.8-nm photodissociation dynamics of formic acid was investigated utilizing degenerate four-wave mixing spectroscopy. The background-free rotational spectrum of the nascent OH radicals was obtained, and a cold rotational energy distribution peaking at $N''=3$ was extracted from the DFWM spectrum. The distribution was well approximated by a Boltzmann distribution with a rotational temperature of $T_{\text{rot}} \sim 716$ K, which corresponds to an average rotational energy of ~ 498 cm^{-1} . The observation of a nonstatistical spin-orbit state distribution, with a preference for the low-energy F_1 manifold, implies the absence of any interactions with nearby triplet states during dissociation. Preferential population of the Λ -doublet was observed, indicating that the ν_7 H–O–C bending vibration in $\text{HCOOH}(\tilde{A})$ and the recoil impulse are the principal sources of the OH rotation. © 2002 American Institute of Physics. [DOI: 10.1063/1.1514587]

I. INTRODUCTION

Photodissociation reactions of organic molecules play a vital role in a number of chemical reactions in the atmosphere. For example, photolysis initiates the chain reactions responsible for ozone-depletion in the stratosphere¹ and contributes to the generation and degradation of toxic (in)organic compounds in the troposphere.² The study of photodissociation phenomena and the related dynamics therefore provides information that can be utilized to understand and predict the molecular reactions in the atmosphere. Such studies also help to elucidate the quantum mechanical electronic structures of molecules in their excited states, because the corresponding processes are closely related to the nature of, and interactions between, the initially prepared excited electronic states.³

The detection of photoproducts is an essential aspect of the investigation of photodissociation dynamics. Several techniques based on nonlinear optical phenomena have been applied to the diagnosis of the atoms and radicals generated by photolysis. In most cases the number densities of the nascent products are quite low; hence, only tools that ensure high signal-to-noise (S/N) ratios are suitable. One nonlinear spectroscopic scheme that has been utilized successfully in several photodissociation studies is degenerate four-wave mixing (DFWM).^{4–6} In DFWM, three input waves with identical frequencies interact in a nonlinear medium to generate a signal with the same frequency.⁴ The spectrally bright signal resulting from a fully resonant process enables the detection of species that are present in low concentrations. The collimated signal can be easily discriminated from un-

wanted noise, yielding a background-free spectrum. The absorption signal response makes it feasible to detect nonfluorescing species.^{4,7} Moreover, from a practical viewpoint this method is easy to implement because it requires only a single-color laser.

Formic acid (HCOOH) is the simplest of the carboxylic acids, which are environmentally important chemical species.^{2,8,9} HCOOH is produced by the oxygenation of organic compounds and is responsible for the acidification of aquatic and terrestrial ecosystems.⁸ In addition, HCOOH is a good source of the formyl radical (HCO), which is an important intermediate in the oxidation of organic compounds in the atmosphere and in the combustion of fossil fuels.⁹ The archetypal nature of HCOOH has led to the extensive study of its photodissociation dynamics.^{10–15}

In the UV region, the C=O bond of HCOOH acts as the main chromophore. Analysis of the UV absorption spectrum of HCOOH shows that the excitation in C=O occurs via the promotion of a nonbonding electron localized on the O atom to the antibonding orbital of the C=O bond, leading to extensive progressions of the ν_3 C=O stretching and ν_7 in-plane O=C–O bending vibrations.^{16,17} The absorption structure beginning at about 260 nm and peaking at 210 nm is assigned to this $^1(n, \pi^*)_{\text{C=O}}$ transition.^{16,17} It has been suggested that the electronic excitation to the $^1(n, \pi^*)$ state is accompanied by a structural change from a planar geometry with C_s symmetry to a nonplanar pyramidal geometry.¹⁶ However, the symbols of A' for the ground state and A'' for the excited state in C_s symmetry still apply because the permutation group is isomorphous with C_s if the molecule easily inverts.¹⁶ Therefore, the electronic correlations associated with each fragmentation route can be deduced within the $A'' \leftarrow A'$ transition regime.¹⁰

^{a)} Author to whom correspondence should be addressed. Electronic mail: khjung@mail.kaist.ac.kr

TABLE I. Energetically possible dissociation pathways of HCOOH upon the excitation to the $^1(n, \pi^*)$ transition (Refs. 10 and 31).

Product channel	ΔH_0
OH+HCO	452 kJ/mol
H+HCOO	389 kJ/mol
H+COOH	433 kJ/mol
H ₂ +CO ₂	35 kJ/mol
H ₂ O+CO	-6 kJ/mol

Upon excitation to the $^1(n, \pi^*)$ state, the energetically possible fragmentation routes include OH radical formation, two molecular eliminations, and two bond-fission channels leading to H-atom formation (Table I).^{10,11} Near 220 nm the dominant primary process is OH formation following C–OH bond scission.^{12,13} At 222 nm, ~70% of HCOOH molecules dissociate to yield OH radicals; the remaining 30% undergo intersystem crossing to the neighboring \tilde{a}^3A'' state, leading to C–H and O–H bond fissions that produce H atoms.^{10,12,13} The OH radicals produced in the photolysis of HCOOH in the region from 220 to 250 nm are characterized by low rotational alignment (μ - J correlation) and recoil anisotropy (μ - v correlation).^{14,15} These low vector correlations are attributed to the force exerted perpendicularly on the reaction coordinate (C–O bond axis) induced by the ν_7 O–C=O bending mode and the torque caused by the structural change following electronic excitation.^{14,15} The nascent OH radicals exclusively populate the $\nu''=0$ level of the electronic ground state.^{14,15,18} A small rotational excitation accompanied by high recoil energy is observed.^{14,15}

In the present work, DFWM spectroscopy was employed to detect the nascent OH radicals produced during room temperature photolysis of HCOOH at 212.8 nm (fifth harmonic of a Nd:YAG laser), which is near the peak of the diffuse absorption band due to the $^1(n, \pi^*)$ transition. The rotational state distribution, relative populations of the two spin-orbit manifolds, and Λ -doublet nonequilibrium were extracted from the background-free DFWM spectrum of the rotational bands of the OH $A^2\Sigma-X^2\Pi$ (0,0) transition. The energy partitioning was analyzed using several dynamical models, and the dynamics of OH-formation from HCOOH exposed to short-wavelength UV radiation is discussed. Inspection of the dynamics of HCOOH should assist our understanding of the behavior of other aliphatic carbonyl compounds.

II. EXPERIMENT

The experimental setup utilized in this work is depicted schematically in Fig. 1. The second harmonic ($\lambda=532$ nm) of a pulsed Nd:YAG laser (Lumonics HY-750) was divided into two parts. One part (with one third of the total output power) was used to pump a dye laser (Lumonics HD-500) containing a dye solution of R640 in methanol (99.9%, Carlo). The dye laser output was frequency-doubled by a KDP crystal. The resultant UV laser beam ($\lambda=304$ – 312 nm) was then divided into three beams using a combination of optical components. The three DFWM beams (*forward-going*, *backward-going*, and *probe*) were of identical intensity and passed through the sample cell in the planar phase-conjugate

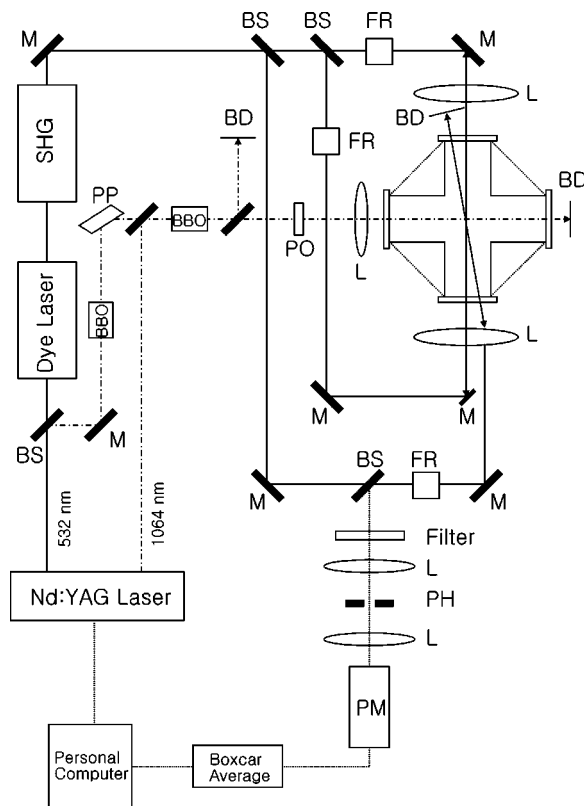


FIG. 1. Schematic diagram of the present experimental setup. PH, L, M, FR, PM, PP, BD, PO, and SHG denote pinhole, lens, mirror, Fresnel rhomb, photomultiplier tube, Pellin–Broca prism, beam dump, polarizer, and second-harmonic generator, respectively.

configuration, as shown in Fig. 1. The sample cell was made of blackened glass. Two lenses of equal focal length ($f=30$ cm) were used to focus the incident DFWM beams into the sample cell, and the three beams crossed one another at the focal point with a matching angle between the *probe* and *forward-going* beams of $\Theta_{\text{DFWM}} = \tan^{-1}(2.5 \text{ mm}/300 \text{ mm}) \sim 0.5^\circ$. Each of the three DFWM beams had a typical power in the range of 0.1–30 μJ (corresponding to an energy density range of 0.6–171 MW/cm^2) at the focal point. The other part of the 532-nm output (with two thirds of the total output power) was used to produce the fifth harmonic ($\lambda=212.8$ nm). First, the light was frequency-doubled using a BBO crystal. Mixing of the resultant fourth harmonic output ($\lambda=266$ nm) with the fundamental output of the Nd:YAG laser ($\lambda=1064$ nm) using another BBO crystal yielded the 212.8-nm photolysis light, which was also focused into the sample cell. The photolysis beam bisected the *forward-going* DFWM beam at a right angle, and the power of the photolysis light was ~ 1 mJ ($5.7 \times 10^3 \text{ MW}/\text{cm}^2$) at the focal point. The delay between the photolysis light and three DFWM beams was controlled by changing the beam paths; the value was fixed at 3 ns to detect OH radicals under collision-free conditions. The resultant signal beam was separated by a beamsplitter and propagated through lenses, a pinhole, and an optical filter to remove interfering scattered light and unwanted fluorescence. The filtered signal was directed into a

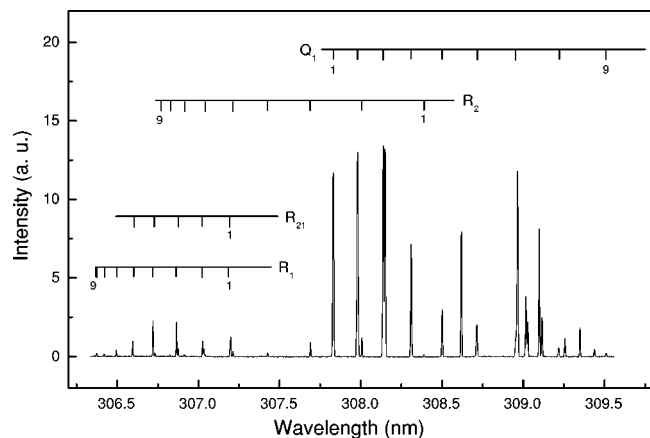


FIG. 2. Background-free DFWM spectrum including several rotational bands of the OH $A^2\Sigma-X^2\Pi(0,0)$ transition after the photolysis of HCOOH at 212.8 nm. All the DFWM beams and photolysis light were horizontally aligned.

photomultiplier tube (Hamamatsu, 1P21) and the amplified signal was averaged by boxcar averagers, which were linked to a personal computer.

HCOOH (98%, Junsei) was purified by vacuum distillation for several hours and degassed through several freeze-pump-thaw cycles prior to use. The purity of HCOOH in the distilled sample was confirmed to be greater than 99% by gas chromatographic analysis. All inlet lines were made of Teflon in order to avoid surface-catalyzed decomposition of HCOOH. Before running the experiment, the sample was flowed through the lines and the sample cell for at least 2 h to deactivate the surfaces. During the experiment the sample was flowed constantly, refreshing the sample during the acquisition of DFWM spectra. Because HCOOH tends to form dimers at high pressures, the pressure inside the sample cell was maintained at <80 mTorr to minimize the number of dimers in the gaseous sample. Based on the absorption cross-section¹⁷ and the equilibrium constant ($K = [\text{HCOOH}]^2/[(\text{HCOOH})_2] = 6.55 \times 10^{16}$ molecules/cm³),¹⁹ it was confirmed that $<1\%$ of OH radicals were generated from the photolysis of the dimer $(\text{HCOOH})_2$. Moreover, several DFWM spectra were obtained in the pressure range of 50–5000 mTorr, but change in the rotational distribution was not apparent.

III. RESULTS AND ANALYSIS

A. DFWM spectrum and signal saturation

Background-free DFWM spectra of some rotational bands of the OH $A^2\Sigma-X^2\Pi(0,0)$ transition were obtained employing the planar phase-conjugate configuration. No interfering signals due to processes such as fluorescence and light-scattering were observed within the limit of the S/N ratios of the present experimental setup, e.g., the S/N ratio was found to be $>15000:1$ for the $Q_1(6)$ branch. The forward-going, backward-going, probe, and photolysis beams were linearly polarized. Figure 2 displays a typical DFWM spectrum, which was obtained with all four incident beams horizontally polarized. The DFWM signal was normalized with respect to the intensities of the probe beam

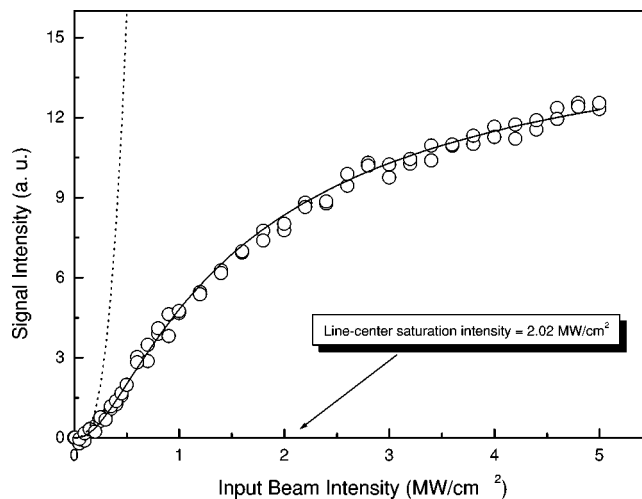


FIG. 3. Saturation of DFWM signal. Open circles denote the signal intensities at the line-center of the $Q_1(6)$ line of the OH $A^2\Sigma-X^2\Pi(0,0)$ transition. The solid line is a curve fitted using Eq. (1). For comparison purposes, the signal behavior without any optical saturation effects is displayed as a dotted line.

using Eq. (1) after the measurement of the signal saturation behavior and the square of the photolysis intensity. The intensity of the probe beam was maintained at $\sim 0.14 \mu\text{J}$, which corresponds to an energy density of 0.8 MW/cm^2 in the present setup (the laser power fluctuated by $<5\%$). Rotational bands peaking at $N''=3$ were clearly observed, indicating that the nascent OH radicals were rotationally cool.

The line-center intensity of the DFWM signal is proportional to the third power of the intensity of the input beam within the low-power regime, and at the high-power limit it does not show any significant dependence on the input beam intensity.^{20,21} In the region between these limits, the relationship between the input beam intensity and the line-center signal intensity is^{20,21}

$$I_{\text{signal}}^0 = 4A \frac{I^3 / (I_{\text{sat}}^0)^2}{(1 + 4I / I_{\text{sat}}^0)^3}, \quad (1)$$

where A is a constant that is determined by the field absorption coefficient and effective optical path length. The parameters I_{signal}^0 , I , and I_{sat}^0 indicate the signal intensity, the intensity of an input beam, and the saturation intensity at the line-center, respectively. In the present study, the saturation intensity at the line-center was obtained by fitting the line-center signal intensities (I_{signal}^0) obtained at various input beam intensities (I) using Eq. (1), as shown in Fig. 3. The curve fitting process yielded an optimal value of $I_{\text{sat}}^0 = 2.02 \pm 0.05 \text{ MW/cm}^2$; the curve obtained by using this value in Eq. (1) is displayed in Fig. 3 as a solid line. This value of the line-center saturation intensity is in good agreement with the value of $\sim 2.0 \text{ MW/cm}^2$ in the literature.²² Given that the experimental intensity of the probe beam was $\sim 0.8 \text{ MW/cm}^2$, it can be concluded that the spectrum in Fig. 2 was obtained at $\sim 40\%$ of the saturation intensity of the $Q_1(6)$ line.

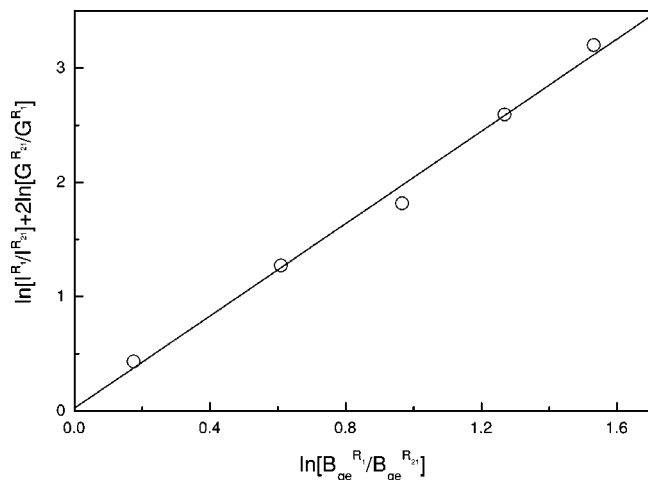


FIG. 4. Log-log plot using Eq. (3) for the nascent OH radicals from the 212.8-nm photolysis of room temperature HCOOH. The intensity of the input beam was $I=0.14 \mu\text{J}$ ($0.8 \text{ MW}/\text{cm}^2$). The linear least-squares fit with $M=2.02$ is displayed as a solid line. The data points represent different values of the rotational quantum number N .

B. Rotational state distribution

The line-center signal intensity is proportional to the square of the population difference, $\Delta N=N_g - [(2J_g + 1)/(2J_e + 1)]N_e$, and to the square of the total geometric factor, G_F^T , as formulated by the relationship²³

$$I_{\text{signal}}^0 \propto \left[N_g - \frac{(2J_g + 1)}{(2J_e + 1)} N_e \right]^2 \times [B_{ge}(N_g, N_e)]^M [G_F^T(\epsilon_4, \epsilon_1, \epsilon_3, \epsilon_2; N_g, N_e)]^2, \quad (2)$$

where N_g and N_e are the populations of the ground and excited states, respectively. B_{ge} represents the Einstein absorption coefficient (the value of which was adopted from Ref. 24), and the analytical expression for G_F^T is given in Ref. 23. The parameter M is a quantity that is related to the degree of saturation of the corresponding transition, and varies from 1 (the strong-field limit) to 4 (the weak-field limit).²³ However, this expression applies only to spatially isotropic ensembles, and care should be taken in its application. Theoretical descriptions of four-wave mixing response in the presence of angular momentum anisotropy have been developed recently by two groups. Vaccaro's group²⁵ and Attal-Trétout's group²⁶ have described the four-wave mixing response using tensor recoupling analyses and a density matrix formalism. However, these theories are difficult to apply directly to the present work because they were developed either under the assumption of the weak-field limit²⁵ or for a different DFWM geometry.²⁶ The signal expressions developed by Vaccaro's group can, however, be reduced to the present form²⁵ for isotropic ensembles. This reduction should be valid for the present work because previous LIF experiments^{14,15} have shown that the quadrupolar tensor component $A_0^{(2)}$ has very small values that scatter about zero with small deviations, which implies that the nascent OH products are almost spatially isotropic. The value of M at a specific degree of saturation can be obtained by comparing

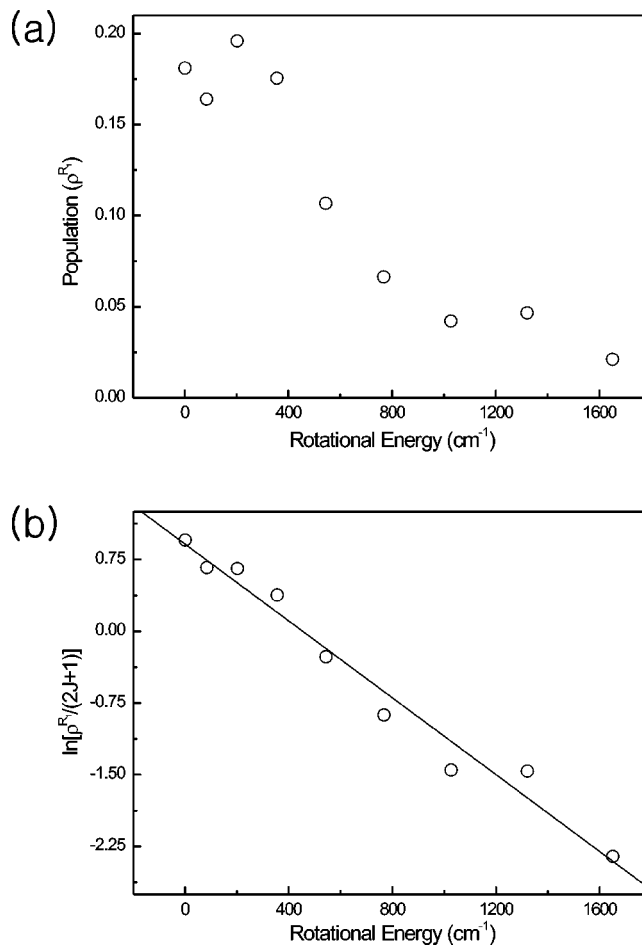


FIG. 5. (a) Rotational state distribution of OH ($X^2\Pi$) radicals probed by the R_1 band, and (b) corresponding Boltzmann plot. The solid line indicates the linear least-squares fit with $T_{\text{rot}}=716 \text{ K}$, which corresponds to an average rotational energy of $E_{\text{rot}}^{\text{ave}}=498 \text{ cm}^{-1}$.

the line-center signal strengths of two rotational lines with a common ground state through the following modification of Eq. (2):^{5,6}

$$\ln \left[\frac{I_{\text{signal}}^{0,R_1}(N)}{I_{\text{signal}}^{0,R_{21}}(N)} \right] = M \ln \left[\frac{B_{ge}^{R_1}(N)}{B_{ge}^{R_{21}}(N)} \right] - 2 \ln \left[\frac{G_F^{T,R_{21}}(N)}{G_F^{T,R_1}(N)} \right]. \quad (3)$$

Thus, the value of M can be obtained as the slope of a least-square fit of this log-log plot. A representative plot is presented in Fig. 4. The input beam intensity was $I=0.14 \mu\text{J}$ (corresponding to an energy density of $\sim 0.8 \text{ MW}/\text{cm}^2$), which corresponds to 40% of the line-center saturation intensity of the $Q_1(6)$ line. The resultant linear least-squares fit gives a slope of $M=2.02 \pm 0.03$. Accordingly, the rotational state distribution for the R_1 band (corresponding to the $X^2\Pi_{3/2}^+$ state of OH) in the lowest vibrational level was extracted using Eq. (2) (Fig. 5).

To test the possibility that the results were influenced by innate errors in the *signal-to-population* conversion process, we additionally measured the DFWM spectrum of OH radicals in a butane/air flame under the same conditions. The flame provides a thermally equilibrated ensemble of OH radicals; thus, a perfect Boltzmann distribution should be obtained if the conversion process is reliable. A Boltzmann

distribution was indeed obtained. Therefore, we could safely assume that the theoretical recipe for the data conversion^{5,6,23} was appropriate.

As shown in Fig. 5(a), the OH radicals are born rotationally cool with a distribution peaking at $N''=3$, implying that a very small portion of the available energy is disposed to the rotational energy of OH. At the same time, no vibrationally excited OH radicals were observed. Based on the S/N ratio of the present setup, <0.5% of the OH radicals seem to be vibrationally excited. A corresponding Boltzmann plot is given in Fig. 5(b). Previous studies carried out in the range of 220–250 nm revealed that the product rotational state distribution of the nascent OH fragments in this region is well characterized by a single Boltzmann rotational temperature.^{13–15,18} We also found that a Boltzmann-type distribution provides a good depiction of the nascent rotational state distribution, as is evident in Fig. 5(b). The solid line in this figure indicates the linear least-squares fit for the Boltzmann plot. As a result, the rotational temperature was determined to be $T_{\text{rot}} \sim 716 \pm 1$ K, which corresponds to an average rotational energy of $E_{\text{rot}}^{\text{ave}} = 498 \pm 1$ cm⁻¹.

C. Nonstatistical spin-orbit state distribution and Λ -doublet nonequilibrium

The electronic configuration of the ground state of OH is $K(2s\sigma)^2(2p\sigma)^2(2p\pi)^3$. In this configuration, three electrons populating the two $p\pi$ orbitals of OH are spatially aligned perpendicular to the molecular (O–H) axis. The unpaired $p\pi$ electron has a spin of $\Sigma = \pm \frac{1}{2}$ and an angular momentum of L ; the projection of L onto the body-fixed z -axis corresponds to $\Lambda = \pm 1$, where $\Lambda = +1$ and -1 correspond to rotational motions with opposing directions. Coupling between Λ (orbital angular momentum) and Σ occurs in OH ($Y=A/B_v = -7.41$, where A is a measure of the strength of the coupling between the spin and orbital angular momenta and B_v is a rotational constant), leading to the splitting of each rotational level into $2|\Sigma| + 1 = 2$ spin-orbit manifolds.²⁷ These two spin-orbit sublevels are designated as F_1 for the $|\Lambda + \Sigma| = \frac{3}{2}$ (${}^2\Pi_{3/2}$) state and F_2 for the $|\Lambda + \Sigma| = \frac{1}{2}$ (${}^2\Pi_{1/2}$) state. The energy splitting between the states is several hundred wave numbers. In this case, for the same N'' the F_1 level (probed by the R_1 band) lies lower than the F_2 level (probed by the R_2 band). The relative population distribution between the two spin-orbit sublevels gives information on the effect of the spin during the photodissociation process, because this distribution is associated with correlations between the potential energy surfaces and the spin-orbit interactions in the exit channels.³ In the experiments reported here, the relative populations of the F_1 and F_2 states were measured as the ratio F_1/F_2 . The statistically weighted ratios are given as a function of N'' in Fig. 6, which shows the statistical distribution as a dotted line. The average value was determined to be 1.38 ± 0.05 indicating that the lower-energy spin-orbit state (F_1) is preferentially populated.

Coupling between the rotational motions of nuclei and electrons is also induced in a rotating molecule. This coupling breaks the degeneracy of each rotational level with a splitting energy on the order of several hundred wave num-

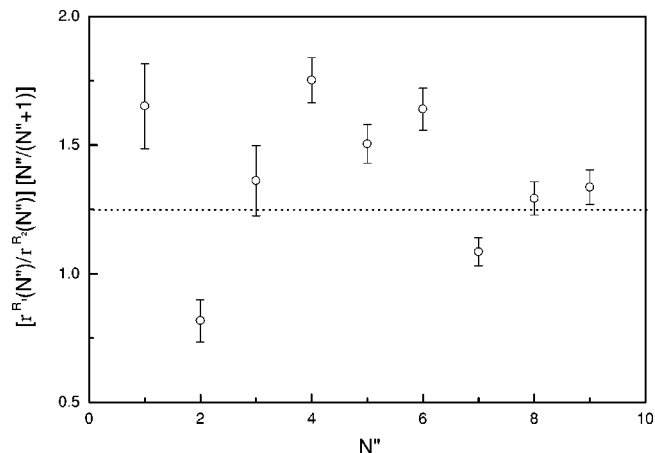


FIG. 6. Spin-orbit state ratios between the $\Pi_{3/2}$ and $\Pi_{1/2}$ states (F_1/F_2) as a function of N'' extracted from the relative populations of the R_1 and R_2 bands. Statistical weights for the individual states were considered. The dotted line indicates the statistical distribution. The nonstatistical distribution shows a preference for the F_1 level.

bers. Each nondegenerate state is defined as either a $\Pi(A')$ or $\Pi(A'')$ Λ -doublet.^{3,28} When the molecule rotates at high speed, the symmetry of the angular momentum is well defined with respect to the nuclear motion. In the high J'' limit, $\Pi(A')$ corresponds to the unpaired $2p\pi$ lobe lying in the plane of rotation, whereas $\Pi(A'')$ corresponds to that aligned perpendicular to the plane of rotation.^{3,28} Since the unpaired $p\pi$ lobe is associated with the covalent bonding orbital (C–O) of the parent molecule, the distribution over the two Λ -doublet states contains dynamical information on the geometry of the electronic wave functions concerned with the photodissociation process.³ The relative distribution between two Λ -doublets can be represented by the ratios of the populations of the R_1 [corresponding to $\Pi(A')$] and Q_1 [corresponding to $\Pi(A'')$] rotational bands. The ratio between the two Λ -doublet states is plotted as a function of N'' in Fig. 7. The values of the ratio were extracted from the relative peak intensities of the R_1 and Q_1 bands. The average value of the

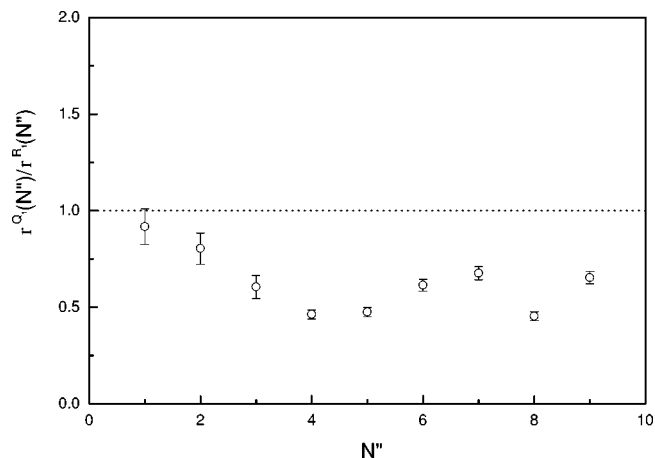


FIG. 7. Population ratios between the two Λ -doublets ($\Pi(A'')/\Pi(A')$) as a function of N'' extracted from the relative populations of the R_1 and Q_1 bands. The dotted line indicates the equilibrium distribution. Nonequilibrium with a preference for the $\Pi(A')$ doublet is observed.

$\Pi(A'')/\Pi(A')$ ratio was 0.63 ± 0.05 , indicating that the $\Pi(A')$ Λ -doublet state is favored. No inversion was observed irrespective of N'' .

IV. DISCUSSION

The UV absorption band of HCOOH starts from 260 nm (the $\tilde{A} \leftarrow \tilde{X}$ band origin is assigned to 259.45 nm) and peaks near 210 nm.^{16,17} This absorption band is attributed to the $\pi^*(10a') \leftarrow n(3a'')$ transition.^{16,17} The transition giving rise to this band is localized on the C=O chromophore, leading to the long progression in the ν_3 C=O stretching vibration.¹⁶ Other progressions pertinent to the ν_7 O=C–O bending motion and a number of unassigned vibrations have also been observed.¹⁶ In addition, four vibrational modes have been observed in a fluorescence excitation spectrum of HCOOH recorded in the 268–257 nm region, i.e., ν_3 C=O stretching, ν_7 O=C–O bending, ν_8 C–H wagging, and ν_9 O–H torsion.²⁹ The activities of the antisymmetric ν_8 aldehyde wagging and ν_9 hydroxyl torsional modes coincide with those of the nonplanar pyramidal structure of HCOOH (\tilde{A}).²⁹ In a study of magnetic field quenching of fluorescence from the $\tilde{A} \ ^1A''$ state in the region 37 200–40 300 cm^{-1} , a sudden decrease in the quenching efficiency was observed above the 3^1 level ($\sim 38\,600\ \text{cm}^{-1}$).³⁰ This behavior has been attributed to predissociation leading to the primary H atom and OH radical formation channels.^{10,14,15,17–19,30} Near the band origin, HCOOH (\tilde{A}) primarily decays nonradiatively but does not dissociate to OH and HCO.³¹ However, the OH formation channel becomes more probable with increasing photon energy. It has been found that the primary dissociation channel yielding OH radicals is the dominant dissociation process in molecules absorbing UV radiation near 220 nm.^{12,15,17–19} A detailed theoretical study has suggested that the H atoms are formed via fission of the C–H (O–H) bond, which is achieved either by passing over relatively high barriers on singlet surfaces or by intersystem crossings to nearby triplet states.¹¹ Scission of the C–O bond is thus the main photochemical process at 212.8 nm, near the center of the $^1(n, \pi^*)$ state.

In the present study, the OH radicals were found to be rovibrationally cold with an average rotational energy of $E_{\text{rot}}^{\text{ave}} \sim 498\ \text{cm}^{-1}$ ($T_{\text{rot}} \sim 716\ \text{K}$). The following relationship was used to determine the fraction of the available energy that is released into the rotational degree of freedom of OH,

$$E_{\text{avl}} = \frac{hc}{\lambda_{212.8}} + E_{\text{int}}^{\text{par}} - D_0^{\text{C-O}}, \quad (4)$$

$$f_{\text{rot}}^{\text{exp}} = \frac{E_{\text{rot}}^{\text{ave}}}{E_{\text{avl}}}, \quad (5)$$

where E_{avl} represents the amount of energy that is available during dissociation; $E_{\text{int}}^{\text{par}}$ indicates the internal energy of the parent molecule at room temperature, which was estimated to be $\frac{3}{2}kT \sim 3.72\ \text{kJ/mol}$; and $D_0^{\text{C-O}}$ denotes the dissociation energy required to break the C–O bond, which was assigned a value of 452 kJ/mol from the literature.³¹ Consequently,

TABLE II. Experimentally determined and theoretically estimated fractions of the available energy that is released into the rotational degree of freedom of OH. Superscript gnd and exc indicate fractions calculated using the geometrical parameters for the ground and excited states of HCOOH reported in Ref. 11. Values in parentheses give the corresponding energies in cm^{-1} .

$f_{\text{rot}}^{\text{exp}}$	$f_{\text{rot}}^{\text{soft,gnd}}$	$f_{\text{rot}}^{\text{soft,exc}}$	$f_{\text{rot}}^{\text{rigid,gnd}}$	$f_{\text{rot}}^{\text{rigid,exc}}$
0.052 (498)	0.023 (216)	0.024 (227)	0.034 (326)	0.036 (342)

$f_{\text{rot}}^{\text{exp}}$ was calculated to be 0.052 (i.e., 5.2% of the available energy flowed into the rotational degree of freedom of OH during dissociation).

The rotational energy of OH can originate from four different sources: (1) thermal energy partitioned in the rotational degrees of freedom of the parent molecule, (2) torque induced by the geometrical change associated with electronic excitation, (3) recoil impulse acting along the C–O coordinate, and (4) zero-point energy of the vibrational quanta of the parent molecule. If the rotational energy of OH originates from the thermal rotational motion of HCOOH, its distribution should be well characterized by a single Boltzmann distribution, as is the case in the present work. In addition, the amount of energy corresponding to the rotational motion of HCOOH is predicted to be $\sim 311\ \text{cm}^{-1}$, which implies a large contribution to the average rotational energy of OH. However, the center-of-mass of OH is located near the O atom, and the angle between C–O and O–H is close to a right angle ($\angle \text{COH} = 108^\circ$ and 109° for *cis*- and *trans*-conformers in the ground state, respectively); hence, all rotational motions of HCOOH defined by x , y , and z molecular axes are hardly transferred to the rotational motion of OH.¹¹ It therefore does not seem plausible that the initial thermal rotational energy in HCOOH is released into the rotational degree of freedom of OH. Similarly, the OH rotation cannot be ascribed to the O=C–O bending torque that is induced by excitation to the $^1(n, \pi^*)$ state.¹¹

When OH is rotationally excited by the recoil impulse along the C–O coordinate, the fraction of the available energy released into the OH rotation can be estimated by using the two radical limits of the impulsive model.³² In the soft radical limit [Eq. (6)], both the vibrational and rotational excitation of fragments is considered to be induced by the recoil impulse. In the rigid radical limit [Eq. (7)], on the other hand, all bonds are assumed to be sufficiently stiff that vibrational excitation can be ignored,³²

$$f_{\text{rot}}^{\text{soft}} = \left(1 - \frac{\mu_{\text{C-O}}}{\mu_{\text{C-OH}}} \right) \sin^2 \chi_{\text{COH}}, \quad (6)$$

$$f_{\text{rot}}^{\text{rigid}} = \left(1 + \frac{I_{\text{OH}}}{\mu_{\text{HCO-OH}} r_{\text{COM}}^2} \sin^2 \chi_{\text{COH}} \right)^{-1}, \quad (7)$$

where $f_{\text{rot}}^{\text{soft}}$ and $f_{\text{rot}}^{\text{rigid}}$ are the fractions expected at the soft and rigid radical limits, respectively. $\mu_{\text{C-O}}$, $\mu_{\text{C-OH}}$, and $\mu_{\text{HCO-OH}}$ are the reduced masses of C and O, C and OH, and HCO and OH, respectively, I_{OH} indicates the moment of inertia of OH, and r_{COM} is the distance from the center-of-mass of OH to the hydroxyl O atom. The geometrical param-

TABLE III. Fundamental frequencies of the ground and excited states of HCOOH. Values are in cm^{-1} .

Symmetry	Mode	Approximate description	Frequency	
			\bar{X}^1A' ^a	\bar{A}^1A'' ^b
A'	ν_1	O–H stretching	3569	(3639.5)
A'	ν_2	C–H stretching	2942	(2962)
A'	ν_3	C=O stretching	1777	1115
A'	ν_4	H–C=O bending	1381	(1336.5)
A'	ν_5	H–O–C bending	1223	(1242.5)
A'	ν_6	C–O stretching	1104	(107.8)
A'	ν_7	O–C=O bending	625	404
A''	ν_8	H–C–O wagging	1033	865
A''	ν_9	H–O–C torsion	642	251

^aReference 35.^bReference 36. Values in parentheses are the averaged values of the frequencies for the *cis*- and *trans*-conformers reported in Ref. 29.

eters of HCOOH were adopted from Ref. 11, and the bond length of ground state OH (0.970 Å) was adopted from Ref. 33. The calculated fractions are listed in Table II. The values for the ground and excited states are presented to show the change in fractions with respect to the equilibrium geometries. No dramatic change in fraction with respect to the structural parameters was observed. On the other hand, vibrationally excited HCO has been observed in a previous study near the band origin.¹³ This may suggest that the vibrational motions in fragments cannot be treated adiabatically, which would imply that the soft radical regime is more appropriate than the rigid radical limit. Since $\angle\text{COH}$ is close to a right angle in the ground state geometry, little vibrational excitation is expected in the soft radical limit. The fact that no vibrationally excited OH has been observed in the present work or previous studies^{13–15,18} is consistent with behavior at

TABLE IV. Fractions of the energies that are transformed from the ν_5 and ν_9 modes of HCOOH to OH rotation, as calculated using Eqs. (8) and (9). Values in parentheses give the corresponding energies in cm^{-1} .

$f_{\text{rot}}^{\nu_5, \text{gnd}}$	$f_{\text{rot}}^{\nu_5, \text{exc}}$	$f_{\text{rot}}^{\nu_9, \text{gnd}}$	$f_{\text{rot}}^{\nu_9, \text{exc}}$
0.031	0.032	0.016	0.006
(296)	(305)	(150)	(60)

the soft radical limit. Therefore, we propose that the recoil impulse is responsible for a rotational energy corresponding to $\sim 2.4\%$ of the total available energy (Table II). This value is much lower than the experimentally determined fraction of $f_{\text{rot}}^{\text{exp}}$, which implies that the recoil impulse is not be the only source of OH rotation. The vibrational motions that can potentially induce OH rotation are ν_5 (the in-plane C–O–H bending vibration) and ν_9 (the out-of-plane OH torsion).^{34,35} Nine vibrational modes and their fundamental frequencies in ground and excited state HCOOH are listed in Table III.^{29,35,36} When the ν_5 bending mode induces OH rotation, the resultant plane-of-rotation lies parallel to the molecular plane of HCOOH. On the contrary, the rotational motion of OH induced by ν_9 torsion has a rotational plane that lies perpendicular to the molecular plane of HCOOH. The Gaussian distribution of the parent bending vibrational momentum is transformed into a Gaussian diatomic fragment rotational momentum distribution, and therefore the overall distribution is characterized by a rotational temperature.³⁴ In order to estimate the amount of vibrational energy that is transformed into the rotational motion of OH, a dynamical model devised for tetra-atomic molecule such as HONO was used.³⁴ Although HCOOH contains five atoms, the negligibly small mass of the H atom allows one to consider this molecule as a quasi-tetra-atomic molecule of structure HOCO,

$$E_{\text{rot}}^{\nu_5} = \frac{\omega_5}{4} \frac{m_{\text{H}}m_{\text{O}}\{r_{\text{C-O}}/m_{\text{H}} - (r_{\text{OH}}\cos\phi_1 - r_{\text{C-O}})/m_{\text{O}}\}^2}{m_{\text{OH}}\left\{r_{\text{C-O}}^2/m_{\text{H}} + (r_{\text{OH}}^2 - 2r_{\text{OH}}r_{\text{CO}}\cos\phi_1 + r_{\text{CO}}^2)/m_{\text{O}} + \frac{r_{\text{OH}}^2}{m_{\text{C}}}\right\}}, \quad (8)$$

$$E_{\text{rot}}^{\nu_9} = \frac{\omega_9}{4} [m_{\text{H}}m_{\text{O}}\{r_{\text{C-O}}\sin\phi_2/m_{\text{H}} + (r_{\text{OH}}\sin(\phi_1 - \phi_2) + r_{\text{C-O}}\sin\phi_2)/m_{\text{O}}\}^2 r_{\text{C=O}}^2] \\ \div [m_{\text{OH}}\{(r_{\text{C-O}}r_{\text{C=O}}\sin\phi_2)^2/m_{\text{H}} + r_{\text{C=O}}^2(r_{\text{OH}}\sin(\phi_1 - \phi_2) + r_{\text{C-O}}\sin\phi_2)^2/m_{\text{O}} \\ + r_{\text{OH}}^2(r_{\text{C-O}}\sin\phi_1 - r_{\text{C=O}}\sin(\phi_1 - \phi_2))^2/m_{\text{C}} + (r_{\text{OH}}r_{\text{C-O}}\sin\phi_1)^2/m_{\text{O}}\}], \quad (9)$$

where m is the mass, r is the bond length, and ϕ_1 and ϕ_2 denote the angles of C–O–H and O–C=O, respectively. The results, listed in Table IV, were calculated based on the geometrical parameters taken from Ref. 11 and the fundamental frequencies given in Table III. This analysis predicts that the zero point vibrational energies of the ν_5 and ν_9 modes in HCOOH contribute $\sim 305 \text{ cm}^{-1}$ ($0.032 \times E_{\text{av1}}$) and 60 cm^{-1} ($0.006 \times E_{\text{av1}}$) to the OH rotational energy, respec-

tively. The main sources of OH rotation are therefore expected to be the ν_5 C–O–H bending mode in HCOOH and the recoil impulse.

The analysis used to explain the moderate rotational excitation can also account for the negligibly small vibrational excitation observed for this system. After excitation, the recoil impulse along the O–H coordinate, and any torque exerted on this coordinate, are very small. As discussed earlier,

TABLE V. Orientation of the unpaired $p\pi$ orbital with respect to the plane of rotation. The values of ϕ_R were calculated using Eq. (10) based on the $\Pi(A')/\Pi(A'')$ ratios in Fig. 7 (Refs. 34 and 37).

N''	1	2	3	4	5	6	7	8	9
ϕ_R	38°	34°	26°	21°	24°	32°	35°	27°	36°

the angle between the C–O and O–H bonds is close to a right angle in both the ground and excited states of HCOOH,¹¹ and consequently the recoil impulse cannot effectively excite the O–H stretching vibration. In addition, the $^1(n, \pi^*)$ transition mainly induces vibrational excitation of the ν_3 C=O stretching mode, and the change in the O–H stretching coordinate is negligible [the O–H bond length of the excited state HCOOH is as large as that of the free OH radical (0.97 Å)].^{11,16,33} The initial transition thus leads to the generation of vibrationally cold OH radicals. This dynamical picture was deduced based on the assumption of fast predissociation on the \bar{A}^1A'' surface.^{13,14} If the dissociation occurs slowly, allowing complete redistribution of energy, the previous vibrational distribution can be calculated using statistical theory. In this case, 11% of OH fragments are expected to be distributed into the $v''=1$ level,¹⁵ which disagrees with the experimental findings presented here and in other studies.^{13–15,18}

A Λ -doublet nonequilibrium in favor of the $\Pi(A')$ state was observed in this work, indicating that the unpaired $p\pi$ lobe of OH lies preferentially in the plane of rotation.^{3,28} This alignment is expected when the rotation of OH is induced by the recoil impulse and the ν_5 C–O–H bending mode in HCOOH because the unpaired $2p\pi$ orbital in the OH fragment is associated with the C–O bonding orbital.^{3,34} The orientation of the $p\pi$ lobe can be expressed in terms of the parameter $\Delta = \langle \cos^2 \phi - \sin^2 \phi \rangle$, where ϕ indicates the angle between the favored plane of rotation and the $p\pi$ orbital.^{34,37} Given the $\Pi(A')/\Pi(A'')$ ratio, the angle ϕ_Λ between the plane of rotation and unpaired $p\pi$ lobe can be deduced:^{34,37}

$$\frac{\Pi(A')_{N''}}{\Pi(A'')_{N''}} = \frac{\cos^2(\phi' - \phi_{\Lambda, N''})}{\cos^2(\phi'' - \phi_{\Lambda, N''})}, \quad (10)$$

$$\phi' = \cos^{-1} \sqrt{\frac{1}{2} + \Delta}, \quad (11)$$

$$\phi'' = \cos^{-1} \sqrt{\frac{1}{2} - \Delta}, \quad (12)$$

$$\Delta = \left\{ 4 + \frac{(Y-2)^2}{(J-\frac{1}{2})(J+\frac{3}{2})} \right\}^{-1/2}, \quad (13)$$

where ϕ' and ϕ'' are the angles between the half-filled $p\pi$ lobe and the plane of rotation for the $\Pi(A')$ and $\Pi(A'')$ Λ -doublets, respectively. $Y = -7.41$ is the ratio of the spin-orbit coupling parameter and the rotational constant.²⁷ The angles calculated using Eq. (10) are collected in Table V. Inspection of Table V leads to an idea that the alignment of the unpaired $p\pi$ orbital is not significant but apparent with angles near 30°. This can be explained in terms of the pyra-

midal geometry of HCOOH in its excited state;¹⁶ the out-of-plane angle in the $^1(n, \pi^*)$ state is $\sim 32^\circ$,¹⁶ which causes the rotational plane of OH to be poorly aligned.

The relative populations between the two spin-orbit manifolds provide information on the contribution of the nearby triplet state or inelastic scattering between the OH and HCO moieties.^{3,34} For the isoelectronic molecule HONO, inversion of F_1/F_2 has been discussed in terms of near-resonant inelastic scattering between the NO and OH fragments and intersystem crossing to the nearby triplet state(s).³⁴ This type of inelastic scattering seems probable because the spin-orbit splittings in $\text{OH}(X^2\Pi)$ and $\text{NO}(X^2\Pi)$ are very similar in magnitude.³⁴ In HCOOH, however, the spin-orbit splitting in HCO is not close to that in $\text{OH}(X^2\Pi)$, leading to the absence of such inelastic scattering. In addition, the HCO fragment has a nonlinear structure, and its angular momentum is quenched during dissociation.¹⁴ Since the F_1 state lies lower than the F_2 state, a preference for the F_1 state is expected unless interactions between the nearby triplet state(s) are involved during the dissociation process. Consequently, the value of $F_1/F_2 \gg 1$ found in the present study indicates that there are no inelastic scattering processes or spin-orbit interactions in the exit channels.

V. SUMMARY

In this study the 212.8-nm photodissociation dynamics of HCOOH was investigated using DFWM spectroscopy. The phase-conjugate configuration, in which the linearly-polarized photolysis light intersects the incident beams at a right angle, was used to obtain background-free rotational spectra of the nascent $\text{OH}(X^2\Pi)$. Both scalar and vector properties of the fragments were extracted from these spectra. The OH rotational energy distribution was well characterized by a Boltzmann rotational temperature of $T_{\text{rot}} \sim 716$ K (corresponding to the average rotational energy of $E_{\text{rot}}^{\text{ave}} \sim 498$ cm⁻¹). No vibrational excitation of OH was observed. The observation of a Λ -doublet nonequilibrium in favor of the $\Pi(A')$ state indicates that the zero point vibrational energy of the ν_5 C–O–H bending mode in the parent molecule and the recoil impulse are responsible for the rotational excitation of OH. The nonstatistical population over two spin-orbit states ($F_1/F_2 \gg 1$) implies that no interaction with nearby triplet state(s) occurs during dissociation.

ACKNOWLEDGMENTS

The authors gratefully acknowledge the Korea Research Foundation for its support (in part) of this research by the nondirected research fund, 1998–2001, and the Korea Institute of Science and Technology Evaluation and Planning by the National Research Laboratory program.

¹M. J. Molina and F. S. Rowland, *Nature (London)* **249**, 810 (1974).

²Peter Brimblecombe, *Air Composition and Chemistry*, 2nd ed. (Cambridge University Press, New York, 1986).

³R. Schinke, *Photodissociation Dynamics* (Cambridge University Press, New York, 1993).

⁴P. H. Vaccaro, in *Nonlinear Spectroscopy for Molecular Structure Determination*, edited by R. W. Field, E. Hirota, J. P. Maier, and S. Tsuchiya (Blackwell Science, London, 1998), p. 75.

- ⁵D.-C. Kim, K. W. Lee, K.-H. Jung, and J. W. Hahn, *J. Chem. Phys.* **109**, 1698 (1998).
- ⁶K. W. Lee, D.-C. Kim, K.-H. Jung, and J. W. Hahn, *J. Chem. Phys.* **111**, 1427 (1999).
- ⁷A. A. Arias, T. A. W. Wasserman, and P. H. Vaccaro, *J. Chem. Phys.* **107**, 5617 (1997).
- ⁸W. C. Keene and J. N. Galloway, *J. Geophys. Res.* **91**, 14466 (1986).
- ⁹Y. Ninomiya, M. Goto, S. Hashimoto, Y. Kagawa, K. Yoshizawa, M. Kawasaki, T. J. Wallington, and M. D. Hurley, *J. Phys. Chem.* **104**, 7556 (2000).
- ¹⁰S. R. Langford, A. D. Batten, M. Kono, and M. N. R. Ashfold, *J. Chem. Soc., Faraday Trans.* **93**, 3757 (1997).
- ¹¹H. Su, F. Kong, W. Fang, and R. Liu, *J. Chem. Phys.* **113**, 1891 (2000).
- ¹²D. L. Singleton, G. Paraskevopoulos, and R. S. Irwin, *J. Phys. Chem.* **94**, 695 (1990).
- ¹³M. Brouard, J. P. Simons, and J.-X. Wang, *Faraday Discuss. Chem. Soc.* **91**, 63 (1991).
- ¹⁴M. Brouard and J. O'Mahony, *Chem. Phys. Lett.* **149**, 45 (1988).
- ¹⁵T. Ebata, T. Amano, and M. Ito, *J. Chem. Phys.* **90**, 112 (1989).
- ¹⁶T. L. Ng and S. Bell, *J. Mol. Spectrosc.* **50**, 166 (1974).
- ¹⁷D. L. Singleton, G. Paraskevopoulos, and R. S. Irwin, *J. Photochem.* **37**, 209 (1987).
- ¹⁸T. Ebata, A. Fujii, T. Amano, and M. Ito, *J. Phys. Chem.* **91**, 6095 (1987).
- ¹⁹G. S. Jolly, D. L. Singleton, and G. Paraskevopoulos, *J. Phys. Chem.* **91**, 3463 (1987).
- ²⁰R. A. Fisher, *Optical Phase Conjugation* (Academic, San Diego, 1983).
- ²¹R. L. Abrams and R. C. Lind, *Opt. Lett.* **2**, 94 (1978).
- ²²G. N. Robertson, K. Kohse-Hoinghaus, S. Le Boiteux, F. Augerre, and B. Attal-Trétout, *J. Quant. Spectrosc. Radiat. Transf.* **55**, 71 (1996).
- ²³S. Williams, L. A. Rahn, and R. N. Zare, *J. Chem. Phys.* **101**, 1072 (1994); S. Williams, L. A. Rahn, and R. N. Zare, *ibid.* **101**, 1093 (1994).
- ²⁴I. L. Childsey and D. R. Crosley, *J. Quant. Spectrosc. Radiat. Transf.* **23**, 187 (1980).
- ²⁵T. A. W. Wasserman, P. H. Vaccaro, and B. R. Johnson, *J. Chem. Phys.* **108**, 7713 (1998).
- ²⁶V. Krüger, M. Dumont, S. L. Boiteux, Y. J. Picard, F. Chaussard, and B. Attal-Trétout, *Phys. Rev. A* **64**, 012716 (2001).
- ²⁷G. Herzberg, *Spectra of Diatomic Molecules* (Van Nostrand Reinhold, New York, 1950).
- ²⁸L. J. Kovalenko and J. B. Delos, *J. Chem. Phys.* **107**, 5460 (1997).
- ²⁹F. Ioannoni, D. C. Moule, and D. J. Clouthier, *J. Phys. Chem.* **94**, 2290 (1990).
- ³⁰H. Abe and H. Hayashi, *J. Phys. Chem.* **98**, 2797 (1994).
- ³¹M. Brouard and J.-X. Wang, *J. Chem. Soc., Faraday Trans.* **88**, 3511 (1992).
- ³²G. E. Busch and K. R. Wilson, *J. Chem. Phys.* **56**, 3626 (1972); G. E. Busch and K. R. Wilson, *ibid.* **56**, 3638 (1972); G. E. Busch and K. R. Wilson, *ibid.* **56**, 3655 (1972); A. F. Tuck, *J. Chem. Soc., Faraday Trans.* **2** **73**, 689 (1977).
- ³³A. A. Radzig and B. M. Smirnov, *Reference Data on Atoms, Molecules, and Ions*, edited by J. P. Toennies (Springer, Berlin, 1985).
- ³⁴R. Vasudev, R. N. Zare, and R. N. Dixon, *J. Chem. Phys.* **80**, 4863 (1984).
- ³⁵J. E. Bertie and K. H. Michaelian, *J. Chem. Phys.* **76**, 886 (1982).
- ³⁶I. C. Hisatsune and J. Heicklen, *Can. J. Spectrosc.* **8**, 135 (1973).
- ³⁷J. H. Shan, V. Vorsa, S. J. Wategaonkar, and R. Vasudev, *J. Chem. Phys.* **90**, 5493 (1989).